Crystal structure of CO-bound cytochrome *c* oxidase determined by serial femtosecond X-ray crystallography at room temperature

Izumi Ishigami[a], Nadia A. Zatsepin[b,c], Masahide Hikita[a,1], Chelsie E. Conrad[c,d,2], Garrett Nelson[b], Jesse D. Coe[c,d], Shibom Basu[c,d], Thomas D. Grant[e], Matthew H. Seaberg[f], Raymond G. Sierra[f], Mark S. Hunter[f], Petra Fromme[c,d], Raimund Fromme[c,d], Syun-Ru Yeh[a], and Denis L. Rousseau[a,3]

[a]Department of Physiology and Biophysics, Albert Einstein College of Medicine, Bronx, NY 10461; [b]Department of Physics, Arizona State University, Tempe, AZ 85287; [c]Center for Applied Structural Discovery, The Biodesign Institute, Arizona State University, Tempe, AZ 85287; [d]School of Molecular Sciences, Arizona State University, Tempe, AZ 85287; [e]Department of Structural Biology, Hauptman-Woodward Institute, State University of New York at Buffalo, Buffalo, NY 14203; and [f]SLAC National Accelerator Laboratory, Menlo Park, CA 94025

Edited by Harry B. Gray, California Institute of Technology, Pasadena, CA, and approved June 8, 2017 (received for review April 5, 2017)

Cytochrome *c* oxidase (C*c*O), the terminal enzyme in the electron transfer chain, translocates protons across the inner mitochondrial membrane by harnessing the free energy generated by the reduction of oxygen to water. Several redox-coupled proton translocation mechanisms have been proposed, but they lack confirmation, in part from the absence of reliable structural information due to radiation damage artifacts caused by the intense synchrotron radiation. Here we report the room temperature, neutral pH (6.8), damage-free structure of bovine C*c*O (bC*c*O) in the carbon monoxide (CO)-bound state at a resolution of 2.3 Å, obtained by serial femtosecond X-ray crystallography (SFX) with an X-ray free electron laser. As a comparison, an equivalent structure was obtained at a resolution of 1.95 Å, from data collected at a synchrotron light source. In the SFX structure, the CO is coordinated to the heme a_3 iron atom, with a bent Fe–C–O angle of ∼142°. In contrast, in the synchrotron structure, the Fe–CO bond is cleaved; CO relocates to a new site near Cu_B, which, in turn, moves closer to the heme a_3 iron by ∼0.38 Å. Structural comparison reveals that ligand binding to the heme a_3 iron in the SFX structure is associated with an allosteric structural transition, involving partial unwinding of the helix-X between heme *a* and a_3, thereby establishing a communication linkage between the two heme groups, setting the stage for proton translocation during the ensuing redox chemistry.

bioenergetics | X-ray free electron laser | crystallography | cytochrome *c* oxidase | serial femtosecond crystallography

In the mammalian respiratory chain, cytochrome *c* oxidase (C*c*O), the final electron acceptor, catalyzes the four-electron reduction of oxygen to water and pumps protons across the inner mitochondrial membrane to establish an electrochemical proton gradient that is used to synthesize ATP. C*c*O contains four redox centers: two heme groups (heme *a* and heme a_3) and two copper centers (Cu_A and Cu_B). Cytochrome *c* delivers electrons to the Cu_A center from which they transfer to heme *a* and then to the heme a_3–Cu_B binuclear center (Fig. 1), where oxygen is reduced to water by using four protons (the substrate protons) from the matrix side of the membrane and four electrons delivered to C*c*O by cytochrome *c*. Associated with the oxygen reduction chemistry, four additional protons (the pumped protons) are translocated from the negative side to the positive side of the mitochondrial membrane. Whereas the mechanism of the O_2 reduction is relatively well understood, the mechanism by which the redox energy is coupled to proton translocation remains unresolved in mammalian C*c*Os (1–4), although it is quite well-defined in bacterial C*c*Os (5, 6).

The determination of X-ray structures of various derivatives of bovine C*c*O (bC*c*O) has been very helpful in understanding many of the features of the enzyme as summarized in a recent review (3). However, the structures obtained with conventional synchrotron light sources were determined from protein crystals exposed to a high X-ray flux and high levels of cryoprotectants at cryogenic temperatures. It has been shown in C*c*O (7, 8) as well as other proteins and enzymes (9, 10) that the high-intensity synchrotron X-ray beam has many deleterious effects including reduction, ligand dissociation, and damage (11, 12). These deleterious effects cause irreversible changes in the protein structure leading to erroneous structural determinations, especially in protein systems containing electron-rich heavy metals (13). In oxidized forms of C*c*O, it has been shown that X-ray reduction of the metal centers occurs even with very short exposures to the X-ray beam (7, 14). Deleterious radiation-induced artifacts are especially evident in the structure of the CO-bound derivatives (bC*c*O–CO) obtained at low temperature by synchrotron radiation in which the X-ray beam has been shown to photodissociate the CO from the heme a_3 iron atom (8). Hence, it is a challenging task to obtain damage-free structures of C*c*O that show its native structure.

To overcome these problems, we have used serial femtosecond X-ray crystallography (SFX), to determine the structure

Significance

A fundamental bioenergetics question is how the redox energy from oxygen reduction in cytochrome *c* oxidase (C*c*O) is coupled to proton translocation. Although crystallography has revealed many properties of the enzyme, the coupling mechanism remains elusive, in part due to artifacts caused by X-ray damage from synchrotron radiation. We determined the structure of CO-bound bovine C*c*O by serial femtosecond X-ray crystallography (SFX) with an X-ray free electron laser, outrunning radiation damage. The SFX structure is compared with the structure obtained with synchrotron radiation in which the Fe–CO bond was cleaved. Our results reveal that ligand binding to heme a_3 triggers an allosteric structural transition that may play a critical role in proton translocation in the C*c*O family of enzymes.

Author contributions: I.I., M.H., P.F., S.-R.Y., and D.L.R. designed research; I.I., M.H., C.E.C., G.N., J.D.C., M.H.S., R.G.S., M.S.H., and R.F. performed research; S.-R.Y. contributed new analytic tools; N.A.Z., S.B., T.D.G., R.F., and D.L.R. analyzed data; and S.-R.Y. and D.L.R. wrote the paper.

The authors declare no conflict of interest.

This article is a PNAS Direct Submission.

Data deposition: Crystallography, atomic coordinates, and structure factors have been deposited in the Protein Data Bank, www.pdb.org (PDB ID codes 5W97 and 5WAU).

[1]Present address: Institute of Materials Structure Science, Synchrotron Radiation Science Division II, Tsukuba, Ibaraki 305-0801, Japan.

[2]Present address: Center for Cancer Research, National Cancer Institute, Advanced Technology Research Facility, Frederick, MD 27102-1201.

[3]To whom correspondence should be addressed. Email: denislrousseau@einstein.yu.edu.

This article contains supporting information online at www.pnas.org/lookup/suppl/doi:10.1073/pnas.1705628114/-/DCSupplemental.

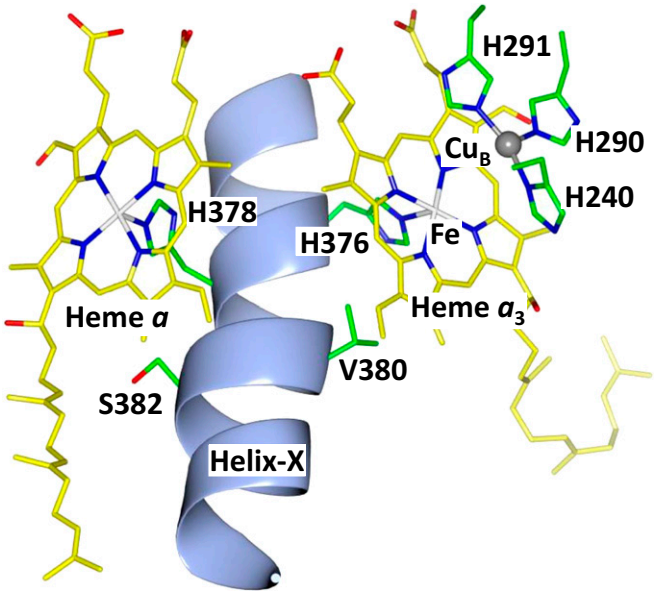

Fig. 1. The heme *a* and heme a_3-Cu_B binuclear center of bCcO. The heme a_3 and heme *a* axial ligands, H376 and H378, respectively, are both located in helix-X, which passes between the two hemes. Cu_B is coordinated by three histidine ligands, H240, H290, and H291. Small molecule ligands, such as O_2, CO, CN, and NO, bind to the heme a_3 iron atom, which is only ~5 Å from Cu_B.

of bC*c*O–CO at room temperature using an X-ray free electron laser (XFEL). SFX has been shown to be a powerful way to outrun conventional radiation damage (15, 16). In SFX, a continuously flowing liquid jet containing a suspension of microcrystals intersects a pulsed X-ray beam from an XFEL before their destruction (i.e., diffraction before destruction) (15). The diffraction patterns are all still snapshots. They are sorted by hit finding with the program Cheetah (17), indexed, and merged into a complete dataset with the program CrystFEL (18, 19), to obtain damage-free room temperature structures of the protein (20). As a comparison with the SFX structure, we also determined the structure of bC*c*O–CO with synchrotron radiation. The comparison of these two structures reveals an allosteric transition involving changes in a critical region of helix-X.

Results

Cytochrome *c* oxidase was isolated from bovine hearts by standard procedures (21, 22). For the synchrotron measurements, large crystals (~300 × 300 × 60 μm) were grown at near physiological pH (pH 6.8). For the SFX measurements, modified crystallization conditions at the same pH were developed to yield microcrystals with a size of ~20 × 20 × 4 μm (*SI Appendix*, Fig. S1). The freshly prepared crystals of oxidized bC*c*O were reduced anaerobically by minimal amounts of dithionite and exposed to CO.

The SFX Structure of bCcO–CO. The SFX data were obtained by injecting a stream of a bC*c*O microcrystal slurry into the vacuum chamber using a gas dynamic virtual nozzle at the Coherent X-ray Imaging (CXI) experimental station of the Linac Coherent Light Source (LCLS) at the Stanford Linear Accelerator Center (SLAC). A typical high-resolution SFX diffraction pattern from CO-bound bC*c*O is shown in *SI Appendix*, Fig. S2. In a total accumulation time of 225 min, 32,651 crystal hits were obtained, from which 26,264 were indexed and merged. The structure was resolved to a resolution of 2.3 Å. The crystals are in space group $P2_12_12_1$ with unit cell parameters of a, b, c = 178.2, 189.8, 209.6 Å, respectively, and α = β = γ = 90°. (See *SI Appendix*, Table S3, for the data analysis and refinement parameters.)

The calculated unbiased F_o–F_c difference map, based on the refinement performed without the CO ligand, shows strong positive density the Cu_B–heme a_3 binuclear center (Fig. 2*A*). In the refined structure with CO modeled in (Fig. 2*B*), the Fe–CO and Fe–His bond lengths are 1.89 and 1.98 Å, respectively, and the Fe–C–O moiety adopts a bent conformation with an angle of ~142° (Fig. 2*C*). Electronically, the Fe–C–O favors a linear geometry that is perpendicular to the heme plane. However, the close proximity of Cu_B to the heme a_3 iron atom in bC*c*O forces the iron-bound CO to move away from Cu_B leading to the bent Fe–C–O conformation, possibly associated with an Fe–CO bond tilted from the heme normal, which cannot be differentiated by the current data.

Structure of bCcO–CO Obtained by Synchrotron Radiation. As a comparison with the room temperature SFX structure, we obtained the bC*c*O–CO structure with synchrotron radiation at 100 K, at the Advanced Light Source (ALS) of the Lawrence Berkeley National Laboratory (beamline 8.2.1). The data collection strategy and analysis are described in *SI Appendix*, Table S3. The structure was determined to 1.95 Å and unit cell parameters of a, b, c = 177.92, 182.55, 208.45 Å, respectively, and α = β = γ = 90° were obtained, similar to those previously reported for the CO-bound enzyme, where data were measured at cryogenic temperatures (178.09, 182.83, 206.93 Å, α = β = γ = 90°) [Protein Data Bank (PDB): 3AG2] with a synchrotron source (SPring-8) (8). They are also comparable to those determined by SFX discussed above, with the exception that the b unit cell axis is 182.55 versus 189.8 Å, which possibly reflects the difference in the data acquisition temperatures.

The exposure of crystals at 100 K to synchrotron radiation, at a total exposure of less than 25 MGy, led to CO dissociation from the heme a_3 iron, as well as its movement toward Cu_B (Fig. 2 *D*–*F*). We define this photoproduct as bC*c*O–CO*. The CO occupies a position in which the Cu–C and Cu–O distances are similar, as shown in Fig. 2*F*. The Cu_B–Fe distance decreased from 5.30 Å, when the CO was coordinated to the heme a_3 iron atom, to 4.92 Å. This change in distance involves primarily movement of Cu_B; the position of the iron atom changes less than that of Cu_B, which changes by ~0.28 Å. This change is a result of the Cu moving from its nearly planar position, defined

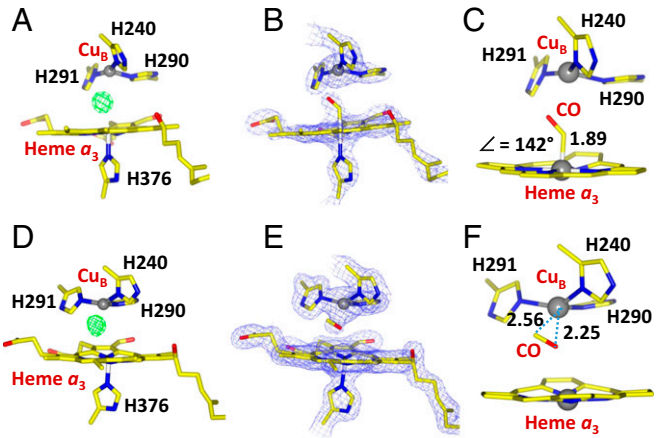

Fig. 2. Active site structures of bCcO-CO and bCcO-CO* obtained with (*A*–*C*) XFEL and (*D*–*F*) synchrotron radiation X-rays. (*A*) Unbiased F_o–F_c difference map (green; contoured at 10 σ), in the absence of the CO ligand showing positive electron density in the binuclear center. (*B*) The $2F_o$–F_c electron density map (blue; contoured at 3.0 σ) of the binuclear center modeled in the presence of the CO. (*C*) Expanded view of the binuclear center. (*D*) Unbiased F_o–F_c difference map (green; contoured at 8 σ), in the absence of CO showing positive electron density near Cu_B. (*E*) The $2F_o$–F_c electron density (blue; contoured at 2 σ) of the binuclear center showing that the CO was photodissociated and located near Cu_B. (*F*) Expanded view of the binuclear center.

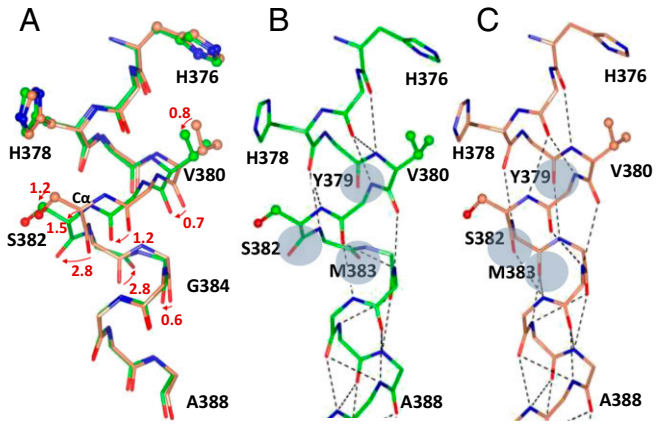

Fig. 3. Allosteric structural transition in the Helix-X fragment induced by ligand binding to heme a_3. (*A*) Superimposed structures of helix-X in bCcO-CO and bCcO-CO* obtained by SFX (green) and by synchrotron radiation (coral), respectively. The arrows designate the [380–384] peptide backbone movements (in Å) induced by ligand binding to heme a_3. In the comparison of the two structures, the Cα carbon atoms of S382 and M383 differ by 1.5 Å, and the backbone carbonyl groups differ by 2.8 Å. Comparison of the alpha-helix hydrogen bonding in (*B*) the bCcO-CO structure obtained by SFX and (*C*) the bCcO-CO* structure obtained by synchrotron radiation. In *C*, in which the CO ligand was dissociated from the heme a_3 iron atom, the normal α-helical H-bonding is established, whereas in *B*, the SFX structure, the α-helical H-bonding patterns of the carbonyl groups of Y379, S382, and M383 are disrupted.

by the three histidine ligands in the CO-bound structure, to an out-of-plane position in the bC*c*O–CO* structure.

Structural Changes in Helix-X. Apart from the differences in the CO position and the Cu_B–heme a_3 distances, the overall structure of the CO-bound and CO-photodissociated proteins were quite similar, except for a section of helix-X. Helix-X is a critical structural element of bC*c*O as it lies between heme *a* and heme a_3 and contains their axial ligands (H378 and H376, respectively) (Fig. 1). In bC*c*O–CO*, the helical structure of this part of the sequence is stabilized by a series of H-bonding interactions between backbone N–H groups and C=O groups located three or four residues earlier along the sequence. In the SFX-based undamaged bC*c*O–CO structure, the [380–384] amino acid fragment is partially unwound due to the disruption of the H-bonding interactions as illustrated in Fig. 3. Specifically, the H bonds between the peptide carbonyls of S382/M383 and their partner residues observed in bC*c*O–CO* are not present, due to a large reorientation of the carbonyls. Similarly, the H bond between the carbonyl of Y379 and the amine group of G384 is not present due to reorientation of the amine group. It is important to note that the [380–385] amino acid fragment constitutes one of the most flexible regions of the bCcO structures, in particular the S382 residue, as evident in the B-factor plots shown in *SI Appendix*, Figs. S3 and S4. The partial unwinding of the α-helical structure of the [380–385] fragment culminates in large movement of the Cα and peptide carbonyl group of S382 by as much as 1.5 and 2.8 Å, respectively (Fig. 3*A*). We define the synchrotron structure with the intact H-bonding interactions as a closed structure and the SFX structure with the disrupted H-bonding interactions as an open structure.

How does ligand binding to heme a_3 trigger the partial unwinding of the helix-X? One might expect that this modulation is a consequence of a change in the position of the helix-X histidine, H376, which is coordinated to heme a_3, where the exogenous ligand binds. Despite the large differences in the backbone between residues 380 and 384, there are only minimal differences (Fig. 3*A*) between residues 376–379, the region that contains the heme axial His ligands (376 and 378). This demonstrates that it is not the histidine movement due to the presence or absence of a ligand on heme a_3 that causes the structural differences. Instead, the differences originate in the interaction of the C pyrrole ring of heme a_3 with residue V380, one of the most common heme face contact residues (23). V380 is the only residue that is in contact with heme a_3 face (Fig. 4) and is part of the region of the helix-X backbone that changes. Upon release of the CO, a heme a_3 distortion brings about the change in position of V380 (*SI Appendix*, Fig. S5).

To quantitate the heme a_3 distortion, we used normal-coordinate structure decomposition (NSD) (24) to analyze the heme structures. In the SFX structure of bC*c*O–CO the composite out-of-plane distortion is 0.603 Å, whereas in the bC*c*O–CO* structure it is 0.866 Å, with the largest changes occurring in the doming (from 0.428 to 0.670 Å) and saddling (from 0.256 to 0.517 Å) coordinates. A full description of the NSD results and descriptions of the doming and saddling structural distortions are presented in *SI Appendix*. The heme distortion results in a 0.5 Å movement of the C_2 and C_3 atoms of the C pyrrole ring of heme a_3, as well as a change in the orientation of the vinyl group attached to it (see the expanded view in Fig. 4 and *SI Appendix*, Fig. S5). Together these conformational changes induce the movement of V380, triggering the partial unwinding of the helix-X structure. Thus, V380 initiates the change in the helix-X structure and transmits the heme a_3 state to the peptide backbone, regulating the open and closed structures.

Discussion

The SFX method was used to determine the structure of bC*c*O–CO, a large membrane-bound protein, without radiation damage and/or photodissociation, at room temperature near physiological pH (pH 6.8). The CO, which serves as a surrogate for the physiological ligand, O_2, binds to heme a_3 in a bent conformation (142°), although a contribution of a Fe–CO bond tilted away from the normal to the heme plane cannot be excluded. A perpendicular orientation of CO with respect to the heme plane is the electronically preferred structure of a heme CO complex due to π-backbonding (25). However, it has been shown in model complexes that a bent conformation occurs when steric factors are present that restrict the perpendicular orientation (26). In the bC*c*O–CO complex, Cu_B lies over the heme plane causing the CO to be bent to 142°, and the Fe–Cu_B distance is elongated to 5.30 Å due to the steric interactions.

In contrast to CO, O_2 is expected to bind to the heme a_3 iron in the same orientation as the CO but without the imposition of

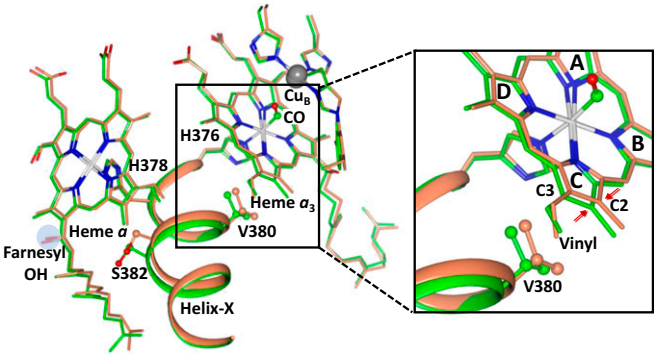

Fig. 4. Helix-X mediated allosteric structural transition induced by ligand binding to heme a_3. Superimposed structures of bCcO-CO and bCcO-CO* obtained by SFX (green) and synchrotron radiation (coral), respectively, showing the ligand binding induced conformational change to the heme a_3, in particular the C-pyrrole ring, and its propagation to heme *a* via the 380–384 residue segment of the helix-X. The farnesyl OH group of heme *a* is highlighted by the blue background. The expanded view shows the interaction region between V380 and the C-pyrrole ring of heme a_3. The red arrows identify the distance change of the C2 atom (0.5 Å) due to the increased heme distortion in the photodissociated state.

steric constraints owing to its sp^2 electronic configuration, which favors a 120° Fe–O–O angle. The absence of steric crowding would also suggest a shorter Fe–Cu_B distance for O_2 compared with CO. In accord with this, in the reduced bCcO–NO complex, in which Fe–N–O adopts an electronically favored bent geometry, the Fe–Cu_B distance (4.92 Å) is short (8). On the other hand, our synchrotron data revealed that CO dissociation from the heme iron leads to the movement of Cu_B toward the heme a_3 iron. The apparent facile change in position of Cu_B, as a function of the ligand coordination on the heme a_3 iron atom, suggests that during the catalytic cycle, Cu_B is able to move in response to the change in the ligation states of the heme a_3, thereby modulating the reactivity of the binuclear center. As suggested recently, a shortening of the Fe–Cu_B distance could play an important role in ligand stabilization (27).

A structure of the CO-bound derivative of bC*c*O was reported by Muramoto et al. (8) in which the crystals were placed in a capillary and measured at room temperature (280 K) by synchrotron radiation. In that structure, CO remained bonded to heme a_3, but the orientation of the CO was reported (8) to be essentially perpendicular with an Fe–C–O angle of 164–168°, in sharp contrast to the 142° we obtained in the SFX measurements reported here. Because the measurements of Muramoto et al. (8) were made with synchrotron radiation, radiation damage may have affected the final structure. In addition, CO photodissociation by the synchrotron X-ray beam would be expected, so the structure may represent a photostationary state, in which the CO was continually being dissociated and rebound to the heme a_3 iron atom.

Allosteric Structural Transition. The data reported here show that ligand binding to the heme a_3 iron is associated with partial unwinding of the helical structure in helix-X generating an open conformation. In both the SFX bC*c*O–CO structure (open) and the synchrotron-based bC*c*O–CO* structure (closed), all four of the metal redox centers are reduced. However, in the former structure, CO is coordinated to heme a_3 whereas in the latter, heme a_3 is ligand-free in a five-coordinate high spin configuration, i.e.,

$$\left(Cu_A^{1+}, Fe_a^{2+}, Cu_B^{1+}, Fe_{a3}^{2+} - CO\right)(\text{open})$$

$$\xrightarrow{\varphi} \left(Cu_A^{1+}, Fe_a^{2+}, Cu_B^{1+}\cdots CO,\ Fe_{a3}^{2+}\right)(\text{closed}). \qquad [1]$$

In Eq. **1**, φ represents photodissociation by the synchrotron radiation beam, and the ⋯ represents the observation that the CO is close to, but not coordinated to, Cu_B. Thus, the removal of ligand coordination of the iron atom on heme a_3 is sufficient to induce the change from the open to the closed conformation and establish the α-helical H-bonding.

Structural differences in helix-X, in various derivatives of bC*c*O (28), and in its bacterial analogs (29), have been reported previously (*SI Appendix*, Table S2). Recently, new high-resolution structures of reduced and oxidized bC*c*O obtained with synchrotron radiation at 50 K were reported (30). To reduce the effects of radiation damage each frame was taken with a 10-s exposure and the crystals were translated by 100 μ after each round of 10 shots. For the measurements, 16 oxidized and 8 reduced crystals were used. In their reduced and oxidized structures, helix-X adopted closed and open conformations, respectively, similar to those defined in this work (*SI Appendix*, Figs. S6 and S7), although in bC*c*O–CO* the helix does not relax all of the way back to the same position as in the fully reduced enzyme, likely due to restrictions imposed by the low-temperature measurements. Inspection of other reported structures of bC*c*O, revealed that when the ferrous heme a_3 iron is in an exogenous ligand-free state, helix-X adopts a closed conformation; conversely, when the heme a_3 iron is coordinated by an exogenous ligand, in either the oxidized or reduced state, helix-X adopts an open conformation. It is notable that the reduced bC*c*O–NO complex has alternate structures (PDB: 3AG3) (8), with helix-X in both the open and the closed structures, possibly due to partial photodissociation of the NO by the synchrotron radiation. (See *SI Appendix*, *SI* Text and Table S2, for a discussion of the helix-X conformations in other derivatives.)

The series of structural changes in the helix-X region induced by ligand binding to heme a_3 (red arrows) are summarized in Fig. 5. Ligand binding to heme a_3 (indicated by a in Fig. 5) leads to a change in the heme distortion (indicated by b in Fig. 5). The change in the heme structure triggers the movement of V380 (indicated by c in Fig. 5), which induces a partial unwinding in helix-X (indicated by d in Fig. 5), causing a reorientation of S382 (indicated by e in Fig. 5). This poises S382 to interact with the OH of the farnesyl side chain, but it is over 8 Å away when heme *a* is reduced. However, during the catalytic reaction, heme *a* alternates between an oxidized and reduced state (gray arrows). When heme *a* becomes oxidized (indicated by f in Fig. 5) the OH of the farnesyl side chain rotates by 160° (indicated by g in Fig. 5) to be within ~3 Å of S382 in the ligand-bound (open) state (*SI Appendix*, Fig. S8). The allosteric structural transition establishes a dynamic communication pathway between the two hemes, offering structural insights into previously proposed proton translocation mechanisms in bC*c*O (1, 4, 28, 31).

In proton translocation studies of bovine and bacterial C*c*Os, three proton channels have been postulated (*SI Appendix*, Fig. S9). The K and D channels connect the negative side of the membrane to the vicinity of the heme a_3–Cu_B binuclear center (32–35), whereas the H channel passes from the negative side of the membrane via the heme *a* center to the positive side (31, 36, 37). Because the catalytic sites of the heme–copper oxidases from eukaryotic and prokaryotic species share the same structural architecture, it has been proposed that the proton pumping mechanism is conserved across species (38, 39). However, this general concept has been questioned by the lack of agreement between those mechanisms shown to be operative in bacterial C*c*Os (5, 6) and those proposed for bC*c*O (1, 4, 28, 31). Illustrative of the distinct properties of the different species is the finding that although a structural change in helix-X, similar to that in bCcO, is seen in *Rhodobacter sphaeriodes* C*c*O (*Rs*C*c*O)

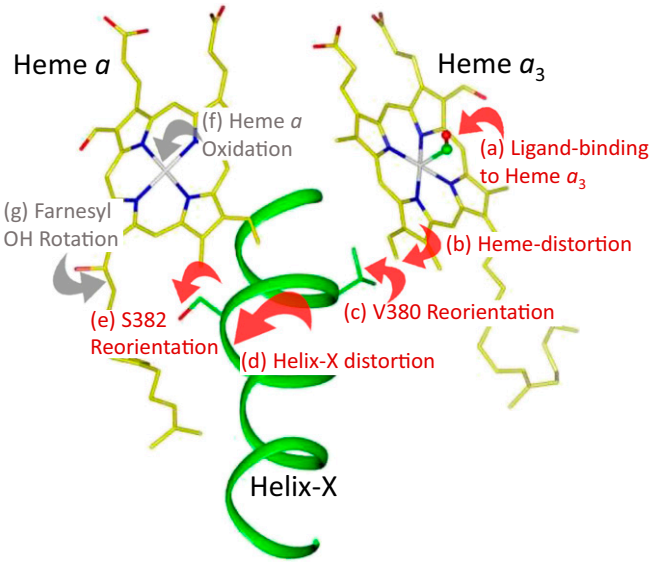

Fig. 5. Cascade of structural changes induced by ligand binding to heme a_3. The letters a–e indicate the sequential structural changes initiated by ligand binding to heme a_3 (red arrows). The letters f and g indicate structural changes induced by the change in the redox state of heme *a* (gray arrows) (31).

(29), the OH group of the heme *a* farnesyl side chain does not undergo the 160° rotation upon the change in the redox state of heme *a* as it does in bC*c*O. Thus, what functional role, if any, the conformation change in helix-X plays in bacterial C*c*Os remains to be determined.

Based on structural and mutagenesis studies of bC*c*O (31), it has been proposed that the H channel is the major pathway for proton translocation in bC*c*O, and the translocation is gated by D51, heme *a*, and the S382 residue/farnesyl side chain OH pair (3). Thus, repositioning of S382 during the allosteric transition plays a critical role in proposed H channel mechanisms (1, 3, 4). Contrary to the H channel mechanisms in the bovine enzyme, extensive mutagenesis, theoretical, and structural studies in bacterial C*c*Os have led to the conclusion that the major proton translocation pathway is the D channel (5, 40, 41). (See *SI Appendix*, *SI Text*, for additional information on the H and D channel mechanisms.) To interrogate the effect of S425 in *Rs*C*c*O (equivalent to S382 in bC*c*O) on proton translocation in the D pathway, Brzezinski and coworkers (42) mutated S425 to alanine and measured its proton translocation efficiency during the O_2 reaction cycle as a function of pH. They found that structural changes in S425 propagate to the D pathway, thereby modulating proton transfer rates (42). These data suggest that the S382-linked allosteric structural transition may play a role in proton translocation in both mammalian and bacterial oxidases.

Ligand Reactivity. It is well established that in solution, following CO photodissociation from the heme a_3 iron atom, the CO first binds to Cu_B; it subsequently dissociates from Cu_B and exits the protein matrix without geminately rebinding to the heme a_3 iron atom (43). This has been postulated as evidence for conformational changes at the binuclear center thereby hindering the CO from rebinding to the heme a_3 iron atom (43). However, our current data do not support this hypothesis, because no structural changes in the binuclear center that can limit the rebinding rate are identifiable in the structure of bC*c*O–CO*.

To better understand the ligand binding/dissociation reactions of bC*c*O, it is necessary to consider the differences between CO and O_2 binding based on the binding reaction scheme shown in Fig. 6, *Inset*, and the corresponding free energy curves. This reaction coordinate is analogous to those derived for the myoglobin reaction with ligands (44). In bC*c*O, for a ligand to bind the heme a_3 iron, it has to first migrate into the protein matrix by overcoming the outer barrier (OB) to form the encounter complex (labeled in gray). Subsequently, it binds to Cu_B by crossing inner barrier 1 (IB-1) and then moves from Cu_B to the heme a_3 iron by crossing inner barrier 2 (IB-2). The initial migration into the protein is expected to be similar for CO (red curve) and O_2 (gray curve), represented by their overlap in the outer barrier. Because the bimolecular binding of O_2 to heme a_3 is over 10^3 times faster than that of CO (45), the inner barriers must be lower for O_2 than for CO. For the CO reaction, IB-2, and possibly also IB-1, is higher compared with the O_2 reaction because in essentially all heme proteins the barrier for binding to the ferrous iron atom is much higher for CO than for O_2 (44, 46). For example, owing to this barrier, in myoglobin the binding rate is 35 times slower for CO than for O_2. Frauenfelder and Wolynes (47) have shown that this difference in the CO and O_2 binding rates in heme proteins is a result of the spin transitions required for the binding of CO to a heme iron atom, which does not occur for O_2 binding.

Consistent with the hypothesized energy curves shown in Fig. 6, Woodruff and coworkers were able to determine that the on rate of CO from Cu_B to the heme a_3 iron is 1,030 s^{-1} (43), at least 35 times slower than the on rate of O_2 from Cu_B (48). In any case, the energy curve associated with the CO reaction indicates that once CO is photodissociated from the heme a_3 iron in bC*c*O, it could either rebind to the heme iron by crossing the IB-2 or escape out of the protein by crossing IB-1 and OB. Which route it takes

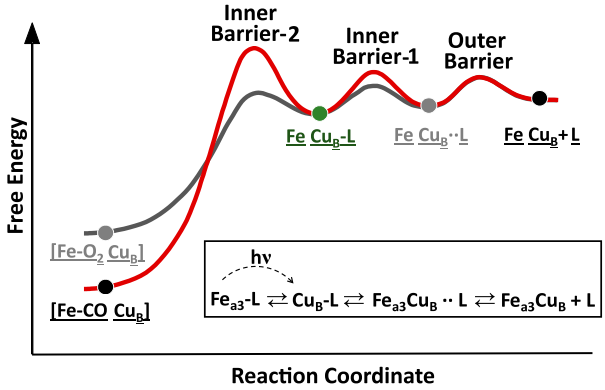

Fig. 6. Schematic illustration of the reaction coordinate for the ligand binding reaction of bC*c*O. The heme ligand, CO or O_2, first enters the protein matrix by overcoming the Outer Barrier to form the encounter complex (FeCuB··L), in which the ligand is loosely associated with the protein. It then binds to Cu_B via passing over inner barrier 1 and subsequently to heme a_3 by passing over inner barrier 2. *Inset* shows the equation for the reversible ligand-binding and photolysis reactions.

depends on the branching ratio R ($R = k_{IB\text{-}2}/k_{IB\text{-}1}$), in which $k_{IB\text{-}1}$ and $k_{IB\text{-}2}$ represent the rate constants for crossing inner barrier 1 and inner barrier 2, respectively. The low branching ratio for CO, due to the higher IB-2 than IB-1 barrier, accounts for the observed low geminate CO recombination yield.

The Inverse Correlation of the Fe–CO and C–O Vibrational Modes. In CO-bound heme proteins, there is a well-established inverse correlation between the frequencies of the Fe–CO and the C–O stretching modes. However, the frequencies of the modes in C*c*O–CO fail to fall on the inverse correlation line; instead, they lie above the line as shown in *SI Appendix*, Fig. S10 (49). It was shown by Yu and coworkers (26) that distortion of the CO, from its typical linear and perpendicular orientation, by distal pocket constrictions, can result in deviations from the correlation curve, in which the data points lie above the curve, possibly due to a reduction in the effective mass of the Fe–C–O moiety due to its bent conformation, thereby modifying the frequencies of the stretching vibrations. The structural data we report here reveal that the Fe–C–O moiety of bC*c*O–CO is bent due to the steric interaction with Cu_B; hence, they offer a molecular explanation for the deviation of the C*c*O data from the inverse correlation line. It is notable that in some studies of C*c*O–CO, a second set of data falling on the inverse correlation line were also observed (49), indicating that in a certain population of the enzyme molecules, Cu_B has moved away from the heme a_3 iron atom, allowing the CO to bind in a linear fashion.

Materials and Methods

Isolation and purification of bCcO from bovine hearts was carried out by standard procedures (21, 22). To generate highly purified bCcO from the isolated enzyme, crystals were formed and harvested. These crystals were redissolved and used as the source for subsequent crystal growth. Large crystals were grown and then crushed to form seed stock to grow microcrystals (~20 × 20 × 4 μm) for the SFX measurements and large crystals (~300 × 300 × 60 μm) for the synchrotron radiation measurements. All crystals were grown in phosphate buffer at pH 6.8 with variable amounts of detergent (decylmaltoside) and PEG-4000, which were optimized for each preparation. For the SFX measurements the crystals were reduced with a minimal amount of dithionite and exposed to CO to form the CO derivative, which was monitored by microscopic spectroscopy. The crystal suspensions were kept at 4 °C throughout and used within a few hours of their preparation. For the synchrotron measurements, the crystals were soaked in ethylene glycol by a stepwise procedure to reach 45% in a CO-saturated buffer. The crystals were immediately frozen and stored under liquid nitrogen for the X-ray measurements.

The SFX experiments were carried out on the CXI instrument at the LCLS at SLAC National Accelerator Laboratory. A gas dynamic virtual nozzle delivered microcrystals, suspended in a liquid jet, to the pulsed XFEL beam at a flow rate of ~10 μL/min. The data were collected at 9.5 keV energy, a pulse duration of 40 fs, and a repetition rate of 120 Hz. The data were sorted, indexed, and merged with the Cheetah (17) and CrysFEL (18) programs and refined with the programs in the Collaborative Computational Project No. 4 (CCP4) suite. The synchrotron X-ray diffraction measurements were carried out at beamline 8.2.1 at ALS with prefrozen crystals of bCcO–CO at 100 K. The data were collected at 12.4 keV, and the full flux was 6×10^{11} photons per s. For premerging of the data, XDS software (50) was used; scaling was done with Aimless, molecular replacement was done with PhaserMR, and refinement was done with Refmac5 from the CCP4 program suite (51). Additional methods and materials details are available in *SI Appendix*.

ACKNOWLEDGMENTS. The SFX experiments were carried out at the LCLS at the SLAC National Accelerator Laboratory. LCLS is an Office of Science User Facility operated for the US Department of Energy Office of Science by Stanford University. Use of the LCLS, SLAC National Accelerator Laboratory, is supported by the US Department of Energy, Office of Science, Office of Basic Energy Sciences, under Contract DE-AC02-76SF00515. Parts of the sample delivery system used at LCLS for this research were funded by NIH Grant P41GM103393, formerly P41RR001209. This work was supported by National Science Foundation (NSF) Science and Technology Center Award 1231306, CHE-1404929 (to D.L.R.), and Division of Biological Infrastructure, Advances in Biological Informatics (ABI) Grant 1565180 (to N.A.Z.) and National Institutes of Health (NIH) Awards GM098799 (to D.L.R.), GM115773 (to S.-R.Y), and R01GM095583 (to P.F.). We also acknowledge support from the Biodesign Center for Applied Structural Discovery at Arizona State University.

1. Ishigami I, Hikita M, Egawa T, Yeh SR, Rousseau DL (2015) Proton translocation in cytochrome c oxidase: Insights from proton exchange kinetics and vibrational spectroscopy. *Biochim Biophys Acta* 1847:98–108.
2. Yoshikawa S, Muramoto K, Shinzawa-Itoh K (2011) Proton-pumping mechanism of cytochrome C oxidase. *Annu Rev Biophys* 40:205–223.
3. Yoshikawa S, Shimada A (2015) Reaction mechanism of cytochrome c oxidase. *Chem Rev* 115:1936–1989.
4. Egawa T, Yeh SR, Rousseau DL (2013) Redox-controlled proton gating in bovine cytochrome c oxidase. *PLoS One* 8:e63669.
5. Kaila VR, Verkhovsky MI, Wikström M (2010) Proton-coupled electron transfer in cytochrome oxidase. *Chem Rev* 110:7062–7081.
6. Wikström M, Sharma V, Kaila VR, Hosler JP, Hummer G (2015) New perspectives on proton pumping in cellular respiration. *Chem Rev* 115:2196–2221.
7. Liu B, et al. (2009) Combined microspectrophotometric and crystallographic examination of chemically reduced and X-ray radiation-reduced forms of cytochrome ba3 oxidase from Thermus thermophilus: Structure of the reduced form of the enzyme. *Biochemistry* 48:820–826.
8. Muramoto K, et al. (2010) Bovine cytochrome c oxidase structures enable O2 reduction with minimization of reactive oxygens and provide a proton-pumping gate. *Proc Natl Acad Sci USA* 107:7740–7745.
9. Hersleth HP, et al. (2007) Crystallographic and spectroscopic studies of peroxide-derived myoglobin compound II and occurrence of protonated FeIV O. *J Biol Chem* 282:23372–23386.
10. Carugo O, Djinović Carugo K (2005) When X-rays modify the protein structure: radiation damage at work. *Trends Biochem Sci* 30:213–219.
11. Sliz P, Harrison SC, Rosenbaum G (2003) How does radiation damage in protein crystals depend on X-ray dose? *Structure* 11:13–19.
12. Sanishvili R, et al. (2011) Radiation damage in protein crystals is reduced with a micron-sized X-ray beam. *Proc Natl Acad Sci USA* 108:6127–6132.
13. Garman EF (2010) Radiation damage in macromolecular crystallography: What is it and why should we care? *Acta Crystallogr D Biol Crystallogr* 66:339–351.
14. Aoyama H, et al. (2009) A peroxide bridge between Fe and Cu ions in the O2 reduction site of fully oxidized cytochrome c oxidase could suppress the proton pump. *Proc Natl Acad Sci USA* 106:2165–2169.
15. Chapman HN, Caleman C, Timneanu N (2014) Diffraction before destruction. *Philos Trans R Soc Lond B Biol Sci* 369:20130313.
16. Chapman HN, et al. (2011) Femtosecond X-ray protein nanocrystallography. *Nature* 470:73–77.
17. Barty A, et al. (2014) Cheetah: Software for high-throughput reduction and analysis of serial femtosecond X-ray diffraction data. *J Appl Cryst* 47:1118–1131.
18. White TA, et al. (2012) CrystFEL: A software suite for snapshot serial crystallography. *J Appl Cryst* 45:335–341.
19. White TA, et al. (2016) Recent developments in CrystFEL. *J Appl Cryst* 49:680–689.
20. Boutet S, et al. (2012) High-resolution protein structure determination by serial femtosecond crystallography. *Science* 337:362–364.
21. Yoshikawa S, Choc MG, O'Toole MC, Caughey WS (1977) An infrared study of CO binding to heart cytochrome c oxidase and hemoglobin A. Implications re O2 reactions. *J Biol Chem* 252:5498–5508.
22. Mochizuki M, et al. (1999) Quantitative reevaluation of the redox active sites of crystalline bovine heart cytochrome c oxidase. *J Biol Chem* 274:33403–33411.
23. Schneider S, Marles-Wright J, Sharp KH, Paoli M (2007) Diversity and conservation of interactions for binding heme in b-type heme proteins. *Nat Prod Rep* 24:621–630.
24. Jentzen W, Song XZ, Shelnutt JA (1997) Structural characterization of synthetic and protein-bound porphyrins in terms of the lowest-frequency normal coordinates of the macrocycle. *J Phys Chem B* 101:1684–1699.
25. Springer BA, Sligar SG, Olson JS, Phillips GN, Jr (1994) Mechanisms of ligand recognition in myoglobin. *Chem Rev* 94:699–714.
26. Yu NT, Kerr EA, Ward B, Chang CK (1983) Resonance Raman detection of Fe-CO stretching and Fe-C-O bending vibrations in sterically hindered carbonmonoxy "strapped hemes". A structural probe of Fe-C-O distortion. *Biochemistry* 22:4534–4540.
27. Sharma V, Karlin KD, Wikström M (2013) Computational study of the activated O(H) state in the catalytic mechanism of cytochrome c oxidase. *Proc Natl Acad Sci USA* 110:16844–16849.
28. Kubo M, et al. (2013) Effective pumping proton collection facilitated by a copper site (CuB) of bovine heart cytochrome c oxidase, revealed by a newly developed time-resolved infrared system. *J Biol Chem* 288:30259–30269.
29. Qin L, et al. (2009) Redox-dependent conformational changes in cytochrome C oxidase suggest a gating mechanism for proton uptake. *Biochemistry* 48:5121–5130.
30. Yano N, et al. (2016) The Mg2+-containing water cluster of mammalian cytochrome c oxidase collects four pumping proton equivalents in each catalytic cycle. *J Biol Chem* 291:23882–23894.
31. Tsukihara T, et al. (2003) The low-spin heme of cytochrome c oxidase as the driving element of the proton-pumping process. *Proc Natl Acad Sci USA* 100:15304–15309.
32. Iwata S, Ostermeier C, Ludwig B, Michel H (1995) Structure at 2.8 A resolution of cytochrome c oxidase from Paracoccus denitrificans. *Nature* 376:660–669.
33. Brzezinski P, Adelroth P (1998) Pathways of proton transfer in cytochrome c oxidase. *J Bioenerg Biomembr* 30:99–107.
34. Brändén M, et al. (2001) On the role of the K-proton transfer pathway in cytochrome c oxidase. *Proc Natl Acad Sci USA* 98:5013–5018.
35. Pereira MM, Teixeira M (2004) Proton pathways, ligand binding and dynamics of the catalytic site in haem-copper oxygen reductases: A comparison between the three families. *Biochim Biophys Acta* 1655:340–346.
36. Tsukihara T, et al. (1996) The whole structure of the 13-subunit oxidized cytochrome c oxidase at 2.8 A. *Science* 272:1136–1144.
37. Yoshikawa S, et al. (1998) Redox-coupled crystal structural changes in bovine heart cytochrome c oxidase. *Science* 280:1723–1729.
38. Gennis RB (2004) Coupled proton and electron transfer reactions in cytochrome oxidase. *Front Biosci* 9:581–591.
39. Pereira MM, Sousa FL, Veríssimo AF, Teixeira M (2008) Looking for the minimum common denominator in haem-copper oxygen reductases: Towards a unified catalytic mechanism. *Biochim Biophys Acta* 1777:929–934.
40. Wikström M (2004) Cytochrome c oxidase: 25 years of the elusive proton pump. *Biochim Biophys Acta* 1655:241–247.
41. Zheng X, Medvedev DM, Swanson J, Stuchebrukhov AA (2003) Computer simulation of water in cytochrome c oxidase. *Biochim Biophys Acta* 1557:99–107.
42. Vilhjálmsdóttir J, Johansson AL, Brzezinski P (2015) Structural changes and proton transfer in cytochrome c oxidase. *Sci Rep* 5:12047.
43. Einarsdóttir O, et al. (1993) Photodissociation and recombination of carbonmonoxy cytochrome oxidase: Dynamics from picoseconds to kiloseconds. *Biochemistry* 32:12013–12024.
44. Carver TE, et al. (1990) Analysis of the kinetic barriers for ligand binding to sperm whale myoglobin using site-directed mutagenesis and laser photolysis techniques. *J Biol Chem* 265:20007–20020.
45. Gibson QH, Greenwood C (1963) Reactions of cytochrome oxidase with oxygen and carbon monoxide. *Biochem J* 86:541–554.
46. Olson JS, Phillips GN, Jr (1996) Kinetic pathways and barriers for ligand binding to myoglobin. *J Biol Chem* 271:17596.
47. Frauenfelder H, Wolynes PG (1985) Rate theories and puzzles of hemeprotein kinetics. *Science* 229:337–345.
48. Blackmore RS, Greenwood C, Gibson QH (1991) Studies of the primary oxygen intermediate in the reaction of fully reduced cytochrome oxidase. *J Biol Chem* 266:19245–19249.
49. Egawa T, Haber J, Fee JA, Yeh SR, Rousseau DL (2015) Interactions of Cu(B) with carbon monoxide in cytochrome c oxidase: Origin of the anomalous correlation between the Fe-CO and C-O stretching frequencies. *J Phys Chem B* 119:8509–8520.
50. Kabsch W (2010) Xds. *Acta Crystallogr D Biol Crystallogr* 66:125–132.
51. Winn MD, et al. (2011) Overview of the CCP4 suite and current developments. *Acta Crystallogr D Biol Crystallogr* 67:235–242.